Monitoring Groundwater Flow in Fractured Rock Environments using Self-Potential Methods

Thesis submitted in accordance with the requirements of the University of Adelaide for an Honours Degree in Geophysics

Matthew Gard

November 2015

THE UNIVERSITY of ADELAIDE

MONITORING GROUNDWATER FLOW IN FRACTURED ROCK ENVIRONMENTS USING SELF-POTENTIAL METHODS

SELF-POTENTIAL STUDY IN FRACTURED MEDIA

ABSTRACT

Self-potential (SP) data has been successfully utilised in porous media environments for mapping groundwater flow, through measurement of surface voltages. Little research has occurred into utilising this method in fractured rock aquifer systems. Such systems are highly heterogeneous in comparison, with groundwater flow focussed along discrete faults, fractures and bedding planes rather than through the bulk matrix as in porous systems. An SP field survey was conducted at Watervale, South Australia in association with a pumping test, with the aim to analyse the viability of this method in this hydrogeological environment. This data was then processed using both a 2D and 3D tomography algorithm, based on the assumption of uniform resistivity due to a lack of a resistivity profile. SP tomography delineated preferential flow directions centred on Line 2, in a NNE-SSW orientation, which was supported through physical drawdown measurements at the associated well. As the dominant fracture and bedding orientations in the region are similarly aligned, it can be assumed the SP response has resolved these discrete fluid pathways. These SP results are encouraging, correlating well with physical observed data and geological information, and support the hypothesis that the SP method has viability for use in fractured rock aquifers.

KEYWORDS

Self-potential, Groundwater, Monitoring, Feasibility, Tomography, Fractured rock

TABLE OF CONTENTS

LIST OF FIGURES AND TABLES

INTRODUCTION

Detecting groundwater flow in the subsurface is typically determined through the use of observation boreholes in the area of interest (Hiscock and Bense 2014). This methodology however requires expensive drilling to create these boreholes, disturbs the natural hydrogeological environment, and only gives point measurements at typically large spacings (Revil et al. 2003, Rizzo et al. 2004, Titov et al. 2005, Maineult et al. 2008). In laterally-uniform clastic sedimentary environments, singular point measurements are sufficient, as the media can be generalised in all directions with some confidence when interpolating and extrapolating the data.

Fractured rock aquifers in contrast, are highly heterogeneous, with high permeability fault, fractures and bedding planes in otherwise low-permeability matrix. Here, flow is almost exclusively through the faults, fractures and bedding planes themselves, as they represent a path of high hydraulic conductivity, with least resistance to flow (Sahimi 2011, Love et al. 2013).

A prospective means for measuring this flow and mapping subsurface ground water movement is through measurement of surface voltages, known as the self-potential (SP) method. Voltages occurring at the Earth surface are the direct result of subsurface generation of electrical current (Revil et al. 2003, Rizzo et al. 2004). The self-potential method is a passive geophysical technique used to measure and interpret these signals, to attempt to resolve the potential current sources at depth (Moore and Glaser 2007). Such sources may be due to a range of subsurface coupling processes, including electrokinetic, thermoelectric and electrochemical (Nourbehecht 1963, Minsley et al.

2007). Typically the electrokinetic response due to groundwater flow, when present, is the major contributor to anomalies observed (Revil et al. 2003, Jardani et al. 2008, Soueid Ahmed et al. 2013), and evaluating the self-potential method for observing this process is the main focus for this study.

Hypotheses based on the current literature suggests physical properties of the near surface materials are conducive to getting measurable voltages at the surface, and that the petrophysical and hydraulic properties and processes occurring in the subsurface are sufficiently understood such that we can make sense of these observed voltages. As the movement of fluid produces a real and detectable electrical potential at the ground surface, it follows, that through processing of the data, we can map the subsurface groundwater flow and derive a meaningful insight into the hydro-geological system in 4D. This method has shown some success in understanding the 4D distribution of groundwater flow in porous media environments, and should show some viability in a fractured rock system.

This report details the methods and outcomes to testing the value of the Self-Potential method in a fractured rock aquifer system. A field test was conducted using a calibrated pump at Watervale, South Australia. At this location, bedding and primary fracturing is steeply inclined. This site had the benefit of multiple, close proximity, observation wells surrounding the pump site, to be used as a method of physical calibration. From this data, information about the hydrogeological system in 4D was to be gathered where possible through computer analysis, and the feasibility of the method examined based on the results.

BACKGROUND

Self-Potential Background

ELECTROKINETIC THEORY

The flow of fluid through a porous medium within the Earth can be responsible, in part, for measurable voltages at the Earth's surface. This is known as the electrokinetic effect, and it is produced fundamentally at the microscopic scale, in the region between the charged grain surface of the Earth material, and the pore fluid (Nourbehecht 1963, Ishido and Mizutani 1981, Revil et al. 1999a, Revil and Jardani 2013).

Nearly all grain surfaces hold a net negative charge (Revil et al. 1999a, Revil et al. 1999b). As a result, positively charged cations present in the bulk electrolyte are attracted to, and adsorbed onto these grains. This attraction sets up what is known as the electric double layer, the region responsible for the production of the electrical response when coupled with pore fluid movement (Morgan et al. 1989, Revil et al. 1999a, Revil et al. 2005, Moore and Glaser 2007, Revil and Jardani 2013).

There are two fundamental boundaries set up in this electrical double layer; The Stern layer, and the Hydrodynamic Shear Plane (Figure 1). The Stern layer is the plane defining the beginning of the diffuse region, or the distance from the grain surface at which charges from the electrolyte are only weakly bound to the grain. In contrast, the Hydrodynamic shear plane is the point at which the pore fluid cations are in motion past grain surface (Revil and Jardani 2013). The region between the shear plane and free-flowing electrolyte is known as the Gouy-Chapman Diffusion layer (Ishido and Mizutani 1981, Morgan et al. 1989, Revil et al. 1999a, Revil et al. 2003).

The interaction of the free-flowing electrolyte and the weakly bound cations of the diffuse region is where the electrical signal is generated. In the presence of electrolyte flow parallel to the hydrodynamic shear plane, the weakly bound excess charges within the Gouy-Chapman Diffusion layer can be dragged in the direction of flow, setting up the movement of charge and the resultant electrical potential (Heinson and Segawa 1997, Revil et al. 2005, Titov et al. 2005, Bolève et al. 2007, Soueid Ahmed et al. 2013). The electrical potential at the hydrodynamic shear plane is known as the zeta potential (ζ), and is often utilised within inversion modelling as the property to characterise the host lithology in an electrical sense (Revil et al. 1999a, Fagerlund and Heinson 2003, Bolève et al. 2007).

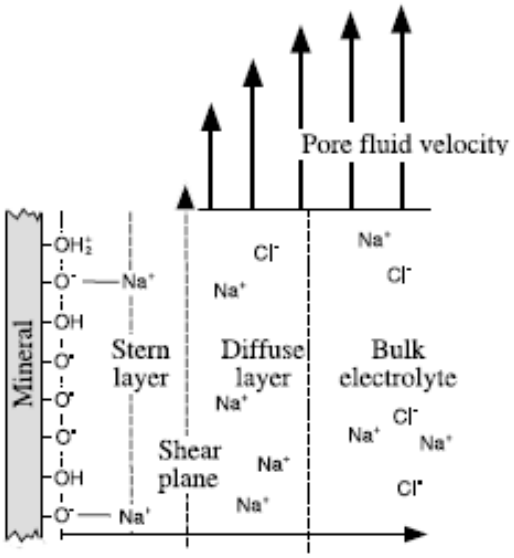

Figure 1: Electrical double layer between the grain interface and the bulk electrolyte (Revil et al. 2003). The interaction of the free-flowing electrolyte and the weakly bound cations of the diffuse region is where the electrical signal is generated.

This process has been described mathematically through an electrokinetic coupling between two fundamental and well understood processes: The electrical aspect (Ohm's Law), and the fluid motion (Darcy's Law).

The general coupled equations for fluid and electric current flow are given by:

$$\boldsymbol{v} = L_{11}\nabla P + L_{12}\nabla\Omega \quad (1)$$

$$\boldsymbol{J} = L_{21}\nabla P + L_{22}\nabla\Omega \quad (2)$$

where $\boldsymbol{v}$ is the fluid velocity through unit area (fluid flux $m.s^{-1}.m^{-2}$), $\boldsymbol{J}$ is the electrical current through a unit area (electrical current density in $A.m^{-2}$), P is the fluid pressure (in Pa or Nm) and Ω is the electric potential (in V), and the L_{xy} values are known as the transport coefficients with constant values. Making some assumptions; that flow is laminar, that the distances between adjacent grain boundaries is much larger than compared with the electric double-layer thickness, and that the electrical conductivity of the pore fluid is much greater than the surface electrical conductivity, these transport coefficients can be given simply as:

$$L_{11} = \frac{-k}{n} \quad (3)$$

$$L_{12} = L_{21} = \frac{\varepsilon\zeta}{nF} \quad (4)$$

$$L_{22} = -\sigma \quad (5)$$

where k is the sediment permeability ($H.m^{-1}$), n is the electrolyte viscosity (m^2s^{-1}), ε is the electrolyte dielectric constant ($F.m^{-1}$), ζ is the zeta potential (V), F is the formation factor (Archie 1942), and σ is the bulk electrical conductivity ($S.m^{-1}$) of the sediment (including the pore space electrolyte).

The coupling is evident in equations (1) and (2), which can be seen to approximate, as $L_{12} = L_{21}$ is very small, the fundamental electrical and velocity equations:

$$\boldsymbol{v} = L_{11}\nabla P \qquad \text{[Darcy's Law equation]} \qquad (6)$$

$$\boldsymbol{J} = L_{22}\nabla\Omega \qquad \text{[Ohm's Law equation]} \qquad (7)$$

(Titov et al. 2005, Moore and Glaser 2007)

ELECTROCHEMICAL & THERMOELECTRIC EFFECTS

Along with the previously discussed electrokinetic effects, other processes can produce an SP response and thus must be considered before making any interpretations. Coupling is also observed in both electrochemical and thermoelectric circumstances (Sato and Mooney 1960, Corwin and Hoover 1979, Revil et al. 2001, Revil et al. 2013). A difference in temperature and/or chemical composition between injection fluids and surrounding country waters, corrosion of the electrode casings and other redox reactions in the subsurface can all lead to the production of an electrical signal, often masked within the overall signature measured at the surface (Darnet et al. 2004, Maineult et al. 2005, Naudet and Revil 2005, Moore and Glaser 2007, Williams et al. 2007).

Typically during pumping tests however, electrokinetic effects are by far the most dominant process in the measured SP signal during the injection phase for sufficiently high pump rates, with the aforementioned electrochemical and other responses potentially only becoming proportionally large enough to be of significance after the cessation of the pumping (Darnet et al. 2004).

Project context and previous SP utilisation

The advantage of the self-potential method is primarily that it is a geophysical method that has inherent sensitivity to the coupling of groundwater to subsurface, is able to be conducted easily and cheaply, and produce a large spatial coverage of dense data points, which proves useful for producing representative models (Revil et al. 2003, Rizzo et al. 2004, Titov et al. 2005).

As well as this, the fact this is a non-invasive, passive geophysical technique ensures data captured is undisturbed. Observation wells are commonly utilised to monitor the hydraulic heads, however the very presence of these wells perturbs the natural hydraulic system, as they are essentially highly permeable pathways for fluid movement (Revil et al. 2003, Rizzo et al. 2004, Titov et al. 2005, Maineult et al. 2008).

Nevertheless, this method has exhibited some difficulties in the literature when interpreting the data recorded. The data are potential fields, and as a result are difficult to uniquely interpret to a map of the subsurface, an issue inherent in all potential field geophysics (Minsley et al. 2007, Jardani et al. 2008).

This method has generally been applied to porous media, and has been shown to be an effective mapping and time monitoring tool (Rizzo et al. 2004, Titov et al. 2005, Revil et al. 2008). Few studies however, have focussed on secondary porosity/fracture rock media systems, and understanding non-homogenous flow in these systems is still limited, largely due to the complexities of such systems.

Geological Setting and the Watervale Oval Site

Watervale is situated in the Northern Mount Lofty Ranges, within the Adelaide Geosyncline, and the region is host to substantial fractured rock aquifers (Costar et al. 2008, Love et al. 2013). Watervale itself is located geologically within the Saddleworth formation; primarily consisting of laminated siltstones, slate and dolomite. The matrix of this formation is typically low permeability, and flow rates are dominated by secondary permeability from fractures, faults and bedding planes. Yields from boreholes in this formation typically yield flow rates in the realm of 0.2 to 2 $L.s^{-1}$, with quite variable salinity levels ranging from sub 500 to 3500 $mg.L^{-1}$ (Love et al. 2013). The groundwater within this unit is used extensively for irrigation in the region.

Flow rates and yields from wells in the area are directly correlated to the orientation and number of fractures, as well as the relative apertures of these fractures allowing fluid to flow (Love et al. 2013).

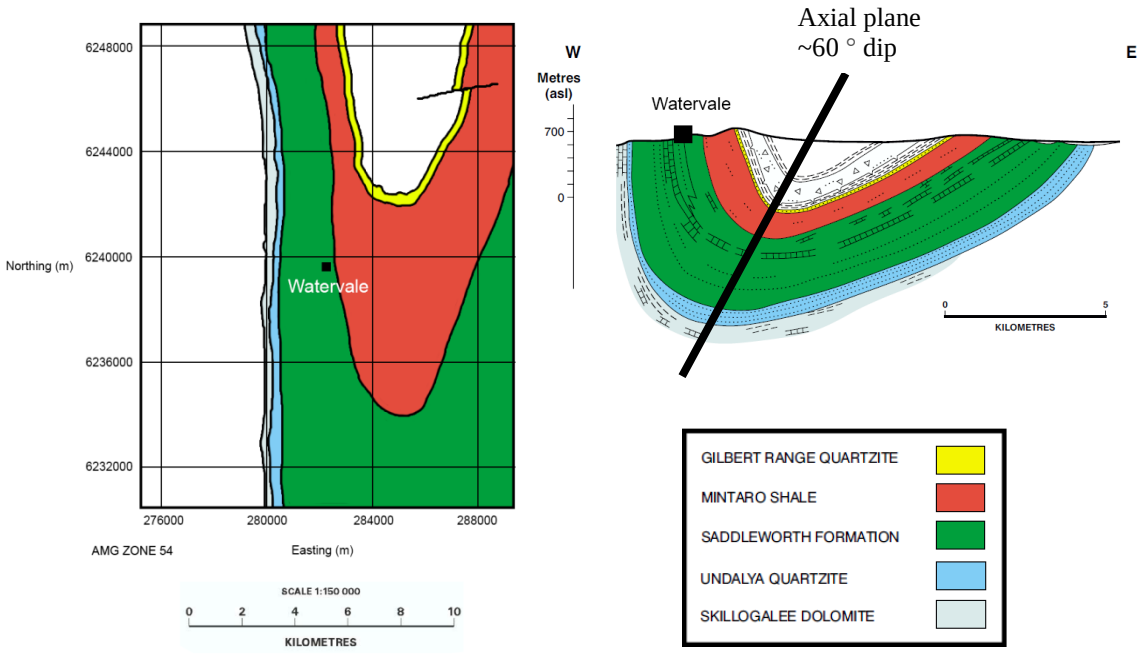

Figure 2: Geological mud map (left) adapted from Love et al. (2013), showing Watervale's relative location with respect to the Nth plunging Hill River Syncline. An east-west cross section (right) through 6244000 mN is presented (Love et al. 2013). Although not through the Watervale section, the relative location of Watervale with respect to the geological units is marked. Steep, near vertical dipping bedding is present at Watervale due to the up going fold limb, and the dominant fracture orientations in the region are parallel to the folds axial plane, also dipping quite steeply at ~60° to the West (right).

As Figure 2 depicts, the Hill River Syncline is the dominant structural feature controlling orientations of fractures and bedding in the Watervale area. Steep, near vertical bedding planes are present at Watervale due to the inclined Western limb of the fold (Figure 2), and the steeply dipping axial plane of the syncline (~60° to the West, N^{th}-S^{th} strike) leads to the dominant fracture orientations propagating throughout the fold at similar dip and strike (Love et al. 2013). The cross section provided is not exactly through the Watervale section, but is used as a representation of Watervale within fold structure with respect to lithological units.

METHODS

Self-potential field logger stations

In the project layout, the 12-channel SP logger systems measure a voltage difference between the electrode station and the reference electrode place ~100m east of the pump well site (in Figure 4). Electrodes were made of stainless steel; non-polarising Pb-$PbCl_2$ electrodes of the 'Petiau' type are generally used (Petiau 2000), but for speed of deployment and the short timescale duration of the pump test, stainless steel appeared to give relatively low noise and electrode drift.

For each electrode this means we measure:

$$\Delta V = V_{SP} + V_{INDUCED} + V_{SOIL} \quad (8)$$

Where ΔV is the measured voltage, V_{SP} is the electrokinetic associated voltage, $V_{INDUCED}$ is the voltages associated with the externally induced electric fields in the area from solar-magnetosphere interactions, and V_{SOIL} are the local voltages associated with the soil environment, including electrochemical variations.

Of these 3 components, V_{SOIL} can be reasonably assumed to be either constant, or changing monotonically at a slow rate, for the duration of the pump test. The difference in redox conditions are believed to account for the mean offsets between individual electrode readings (a localised, constant effect).

These measurements were achieved by utilising modified seismic cables and jumper leads on the take-outs of the cable connected to the stainless steel electrodes. The SP field logger box was connected to both a battery power source as well as solar panels to ensure power was supplied throughout the tests.

The logger comprised of the DataTaker85, which is a 24-channel system 16-bit A/D with automatic gain ranging with a least count of about 10μV for each differential input for a dynamic range of 300μV. Sampling was set at 1s because there is little natural induced signal in the bandwidth of 1-10s, and hence aliasing is not a significant problem. The logger channels are of the Sigma-Delta style, and thus average over many samples at a higher clock rate. The logger does not have GPS synchronisation, but drift rate is less than a second over a day.

Figure 3: SP field logger set up used for the survey. The SP data taker box (centre) is connected to both a battery power source as well as solar panels (either side) to ensure power is supplied throughout the test. Modified seismic cables are utilised (black cable); with the modified jumper lead connectors seen in the foreground being attached to the metal stakes acting as electrodes in the ground. An individual SP field logger was utilised for each line.

Self-potential survey

Four pumping tests were conducted over the course of two days, from the 9th to the 10th of September, 2015, in conjunction with the Department of Environment, Water and Natural Resource, South Australia, at the Watervale Oval site.

48 of these metal stakes were laid out, with 12 assigned to each line. Each line ran alongside or directly towards the observation wells on the site, radially outwards from the central pump well. At each of these boreholes we could monitor the physical drawdown of the water table, and use this as direct physical data for comparison to the SP signals recorded.

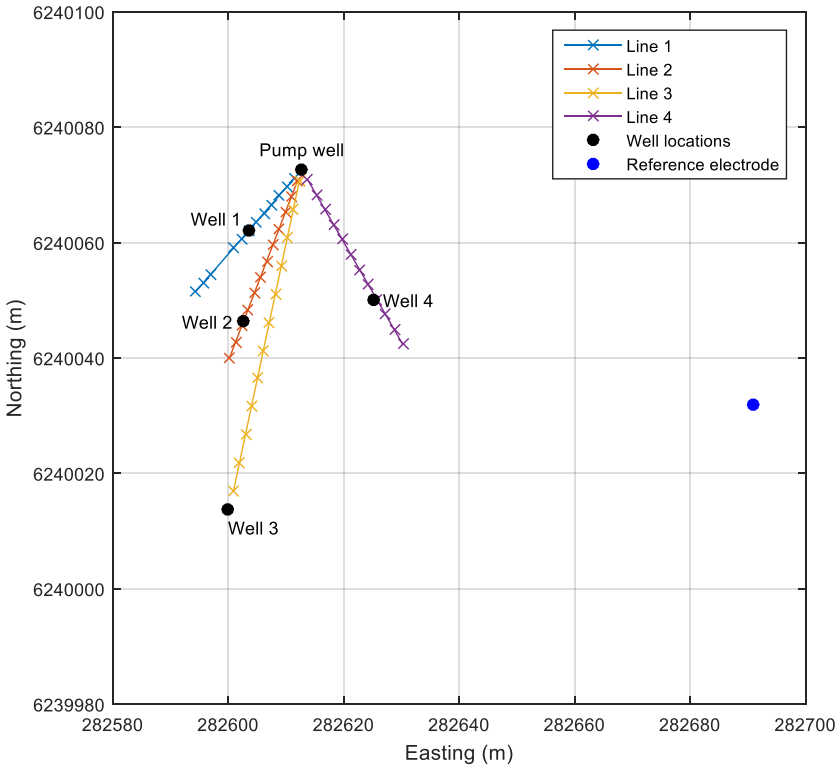

Figure 4: SP line configuration for the Watervale survey. Each cross denotes the location of an electrode, and each colour the separate lines. Also noted are the well locations at the site, and the lines ran past these. ~100m to the east was the location of a small cluster of 4 reference electrodes, ideally far enough away to as not be affected by the pump test.

The lines began 2m from the pump well, as to be out of the way for the pump field officer to conduct the test. Lines were labelled 1 through 4 in a counter clockwise direction. Orientations of these lines would have preferably been in a radial pattern in all directions, however due to site limitations, this was not the case, and we were limited to a smaller angle of observation wells.

The lines were oriented at 221, 201, 192, and 150° N (Geographic) respectively, with the spacing between electrodes varying for each line. Line 1 was spaced at 2m intervals between electrodes with one 6m interval between stakes 9 and 10 to cross a small gravel road. Lines 2 and 4 were spaced at 3m intervals and Line 3 at 5m intervals, in an attempt to have the end electrode as close as possible to the more distant observation well.

Approximately 100m east of the wells, one stake was placed for each box, within a small area, to act as reference electrodes. The idea is that these reference electrodes are placed sufficiently far away such that they show no interference as a result of the pump test itself, and only record natural background voltages throughout the test.
On the 9th of September 2015 (day 1), the first test began at 14:00:00 (Australian Central Standard Time) with an average pump rate of ~1.1L.s^{-1}, and was conducted for 40 minutes. Around 1:10:00hrs later, after a recovery period, pumping was resumed and maintained an average pump rate closer to ~0.75 L.s^{-1} for around 35 minutes, concluding at 16:45:00. (Figure 5)

Physical drawdown of the water table was measured in all wells before, during, and following cessation of the pumping, with values recorded every 5 minutes (Figure 5 & Appendix D).

OBSERVATIONS AND RESULTS

Day 1 data is the main focus for the following results and discussion, as this appeared to be the most promising data, with particular focus on the first pumping period.

Well 2 was the only observation well to show any significant variation in drawdown associated with the pumping test (Figure 5)

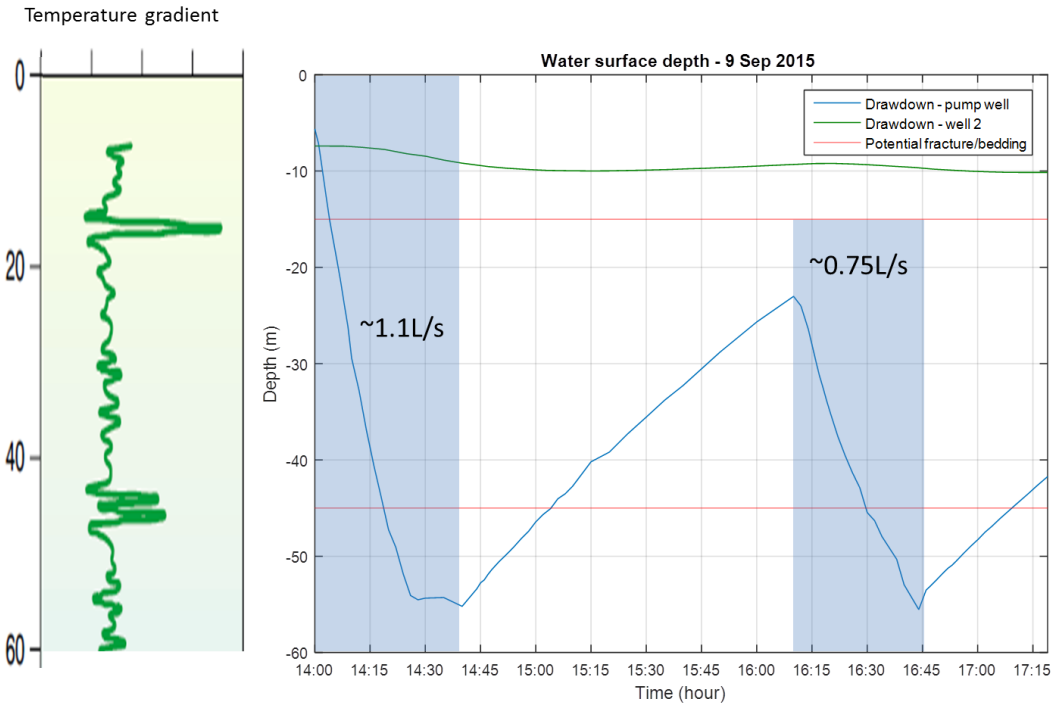

Figure 5: Drawdown in pump well as a function of time. Periods of pumping marked by shading. Initial pump rates average around 1.1L/s for the first test, and 0.75L/s for the second, on day 1. Full recovery was not achieved between the pumps. To the left of the drawdown plot, a temperature gradient profile used from Love et al. (2013) for a well in Watervale, with peaks believed to correspond with discrete flow pathways. Although not the same well, as an example this shows the fact that potentially major flow paths were in a state of flow for the entire period between pumps (marked as an example in red lines). Drawdown from well 2 is also shown in green.

Figures 6 to 9 show the data from the four loggers from 13:30 to 17:10, which encompasses both of the pump periods shown in Figure 5. The voltages have been median-filtered with a filter length of 60s to effectively low pass the data set for noise at periods less than one minute. A linear trend was removed and the data are plotted as stacked sections offset by 10 mV for Lines 1-3, and 2 mV for Line 4.

The linear trend effectively removes voltages that arise due to polarisation effects at each electrode and diurnal-scale changes in soil moisture and temperature. Typically these were of very low order of less than a few mV per hour. The absolute voltage reading are not the information of interest, instead the variations of voltage from background baseline values.

Electrodes that were particularly noisy were removed from the stack.

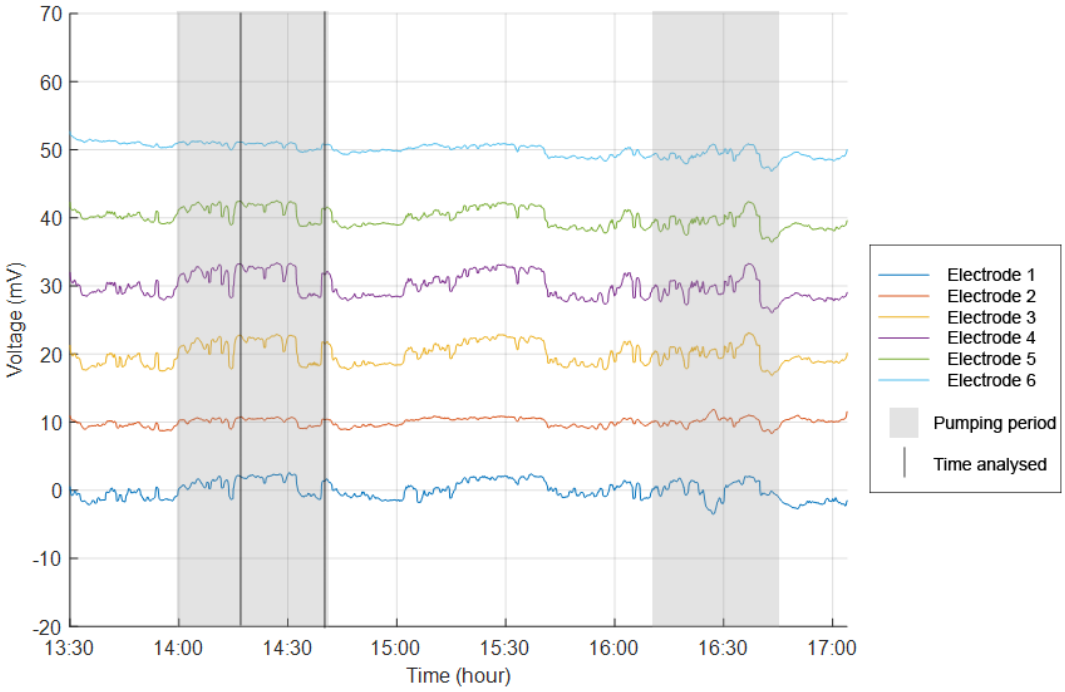

Figure 6: SP Line 1 data from electrodes 1 through 6, mean corrected and then manually shifted for easier viewing.

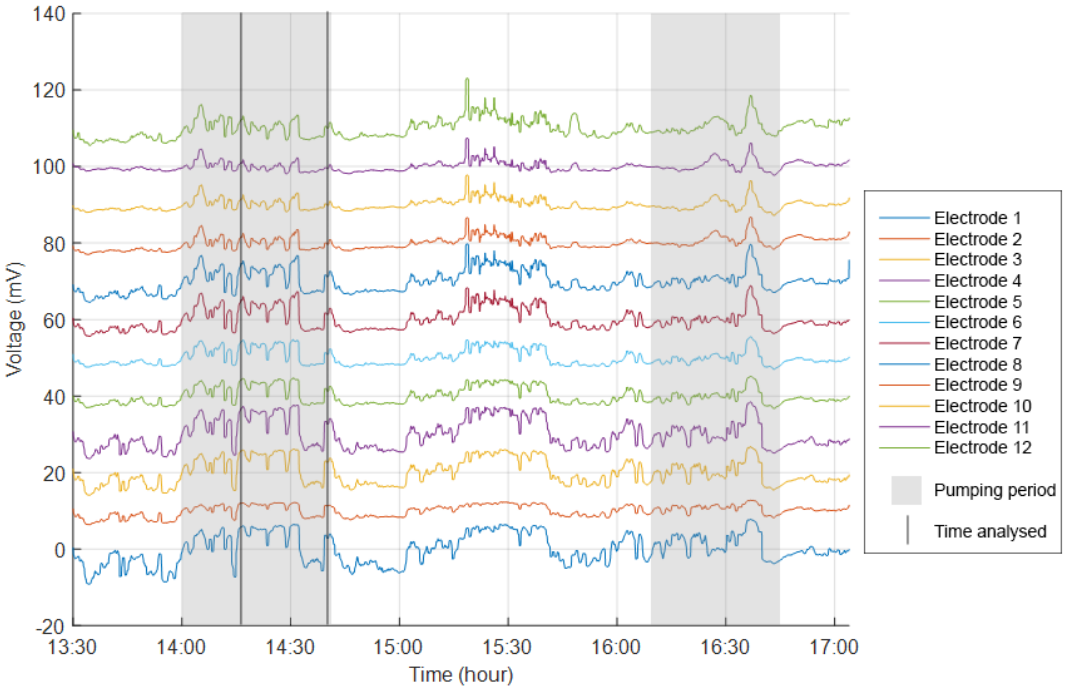

Figure 7: SP Line 2 data from electrodes 1 through 12, mean corrected and then manually shifted for easier viewing.

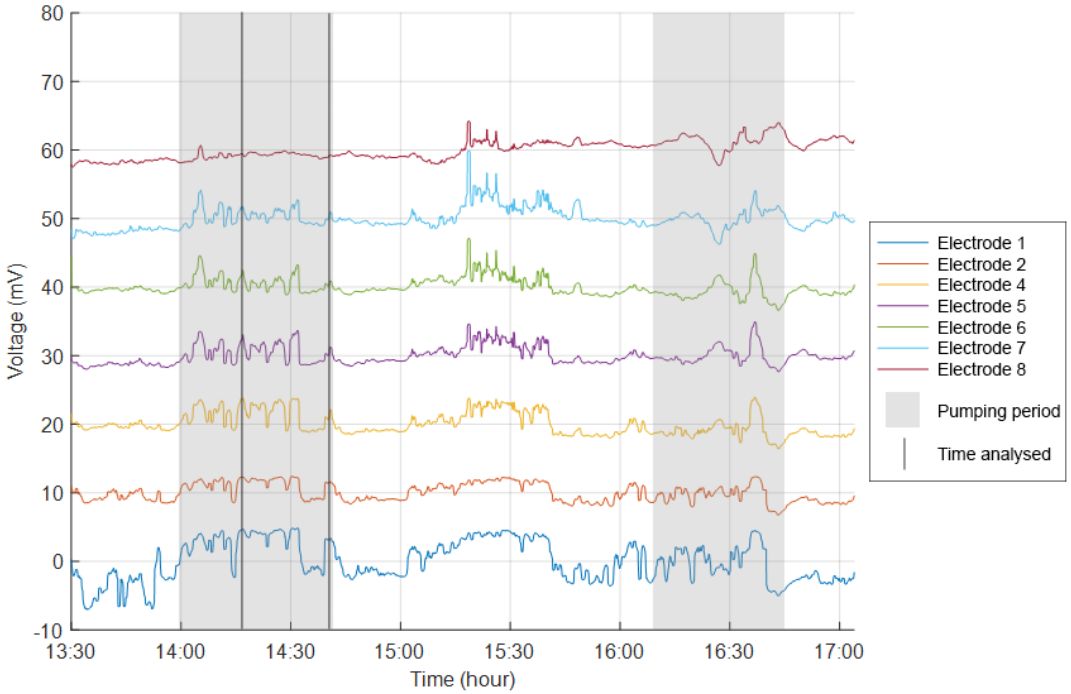

Figure 8: SP Line 3 data from electrodes 1 through 8, excluding 3, mean corrected and then manually shifted for easier viewing.

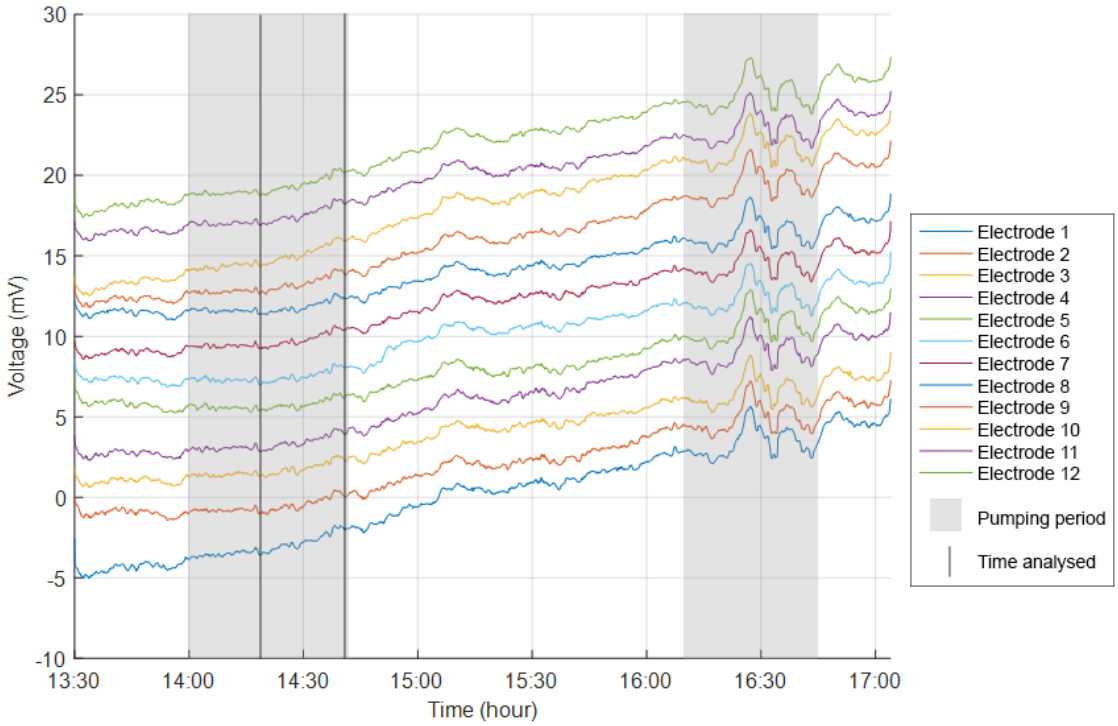

Figure 9: SP Line 4 data from electrodes 1 through 12, mean corrected and then manually shifted for easier viewing.

Although an extensive data set, only discrete time intervals can be analysed in any detail in this report. Data from the first pumping period, from 14:00:00 to ~14:44:00 on the 9th of September, became the focus for this example. This pump was the most undisturbed hydrogeological environment, for a reasonable length first pump, with the highest pump rate of all the tests done over the two days. Two regions of signal within the first pump test, around the early-mid stage, as well as the end of the first pump test, were focussed on.

Early-mid stages of pumping: 9th Sept @ ~14:20:00

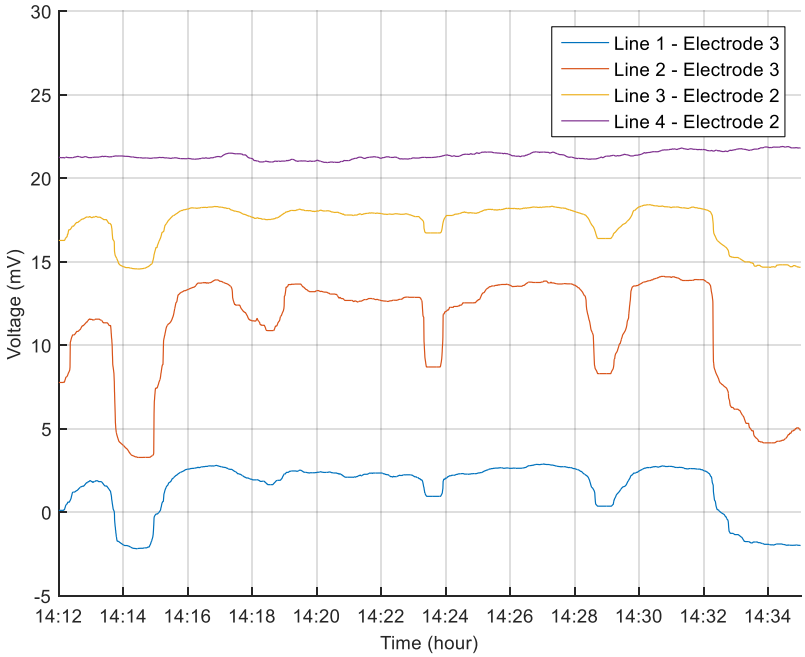

Figure 10: Relatively proximal electrodes from each line are graphed around the early to mid-stages of the first pumping session @14:40:00. See Figure 4 – map of site for electrode locations. Line 2 shows greater amplitude than Lines 1 and 3, which appear to be relatively similar. Line 4 shows very little amplitude change.

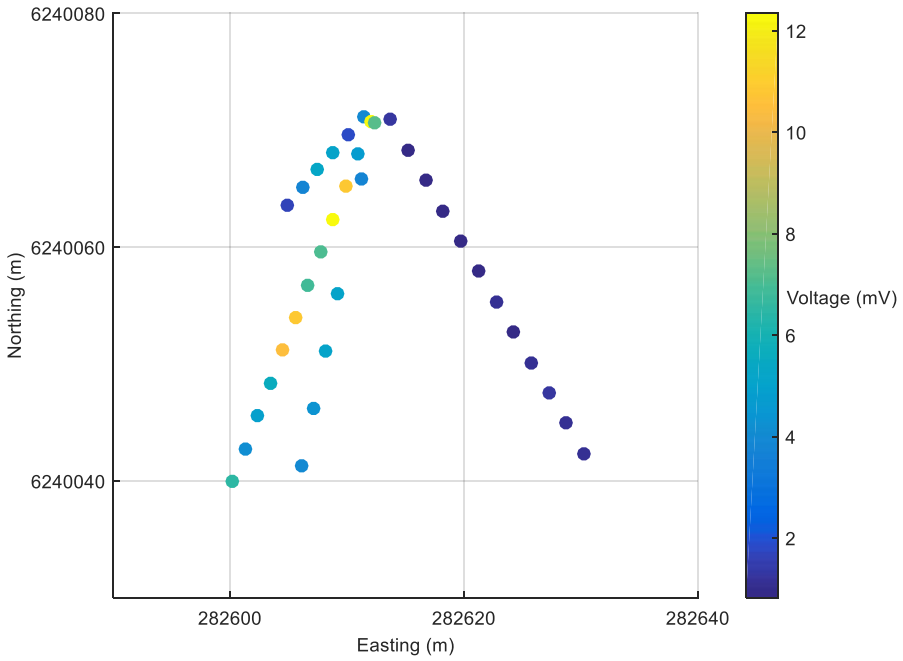

Figure 11: Voltage differences from baseline are plotted at the early-mid stage of pumping for each line @14:20:00. A map representation – clearly defining increased voltages along Line 2.

Late stages of pumping: 9th Sept @~14:40:00

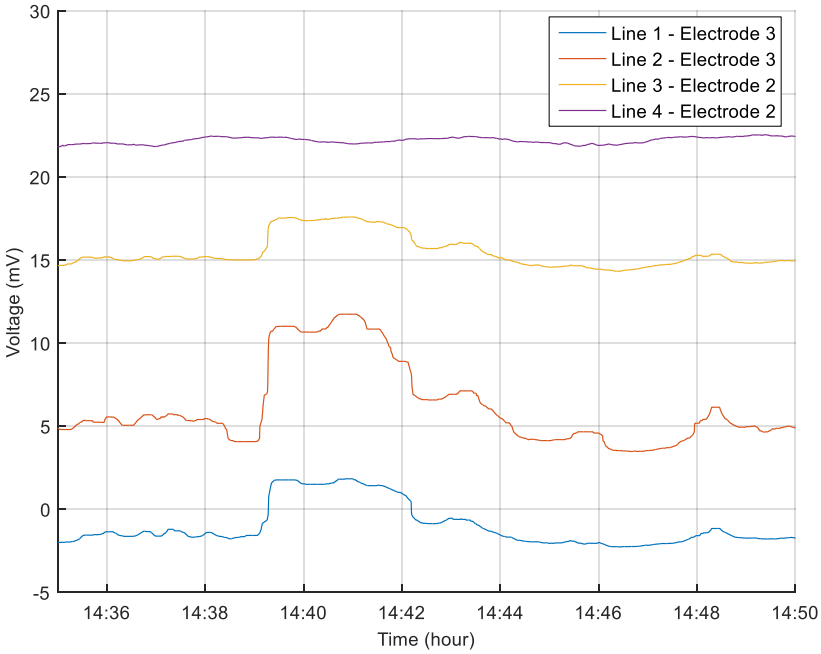

Figure 12: Relatively proximal electrodes from each line are graphed around the early to mid-stages of the first pumping session @14:40:00. See Figure 4 – map of site for electrode locations. Line 2 shows much greater amplitude than Lines 1 and 3, which appear to be relatively similar. Line 4 shows very little amplitude change.

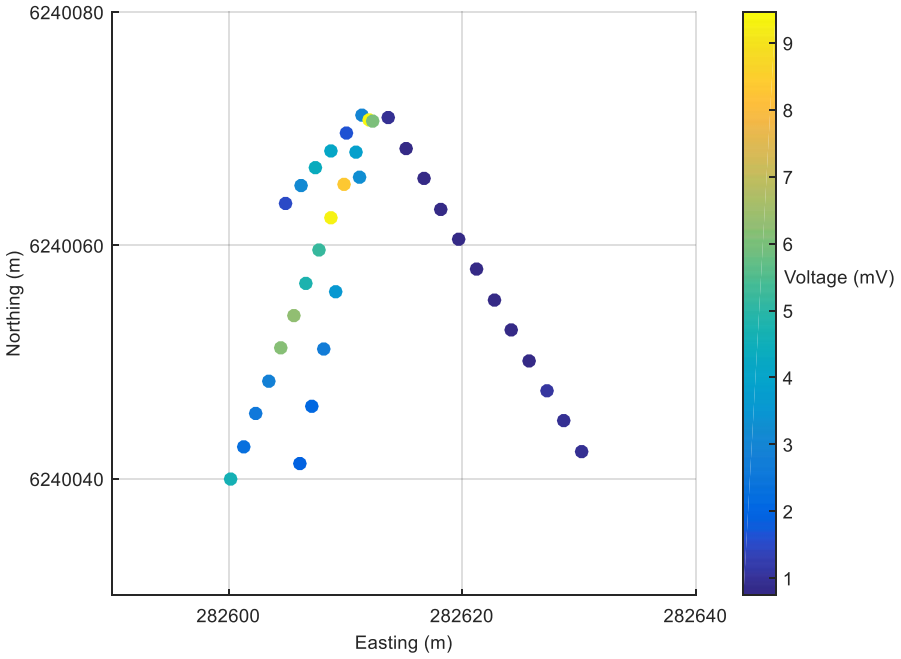

Figure 13: Voltage differences from baseline are plotted at the late stage of pumping for each line @14:40:00. A map representation – clearly defining increased voltages along Line 2, but of lower amplitude than that of Figure 11 at the early time of the pump.

For both intervals analysed, the proximal electrode plots give confidence that the data measured was relatively accurate. Different lines, boxes, and electrodes have come together to record strongly similar signals. Line 2 was chosen to be the main focus for 2D tomography analysis as it showed at nearly all time intervals, the greatest amplitude in voltage response from baseline, as well as the fact well 2 recorded the greatest drawdown in the piezometers than any of the other wells (~2.5m whereas the other wells only recorded cm scale movement). See Appendix D for drawdown information.

Data processing and Tomography

To interpret SP data, requires a means of mapping the spatial distribution of surface voltages with sub-surface electrokinetic sources. As with all potential field data, the problem is non-unique and undetermined. One simple approach to attempt to define the lateral and depth coordinates of the anomalies is through SP tomography.

Tomography is an image reconstruction approach that calculates a map of likelihoods for the locations of the SP sources – e.g. (Di Maio and Patella 1994, Hämmann et al. 1997). In this project, the approach of Hämmann et al. (1997) was used. Modifications were made to calculate absolute potentials (rather than the electric fields) and to generalise their method from a two-dimensional line-source to a point-source to two and three-dimensional Earth.

The algorithm consists of three main steps, for both the 2D and 3D cases.

First, a volume scan of elementary point sources is conducted through the desired region. To do this, a scanner function $g(x_i, x, z)$, and $g(x_i, y_j, x, y, z)$ is defined (for the 2D and 3D case respectively). This scanner function represents the potential component at the electrodes on the surface [(x_i) or (x_i, y_j)], due to an elementary source located at position [(x, z) or (x, y, z)]:

$$g(x_i, x, z) = \frac{1}{(x_i - x)^2 + (z)^2} \qquad \text{(2D)} \qquad (9)$$

$$g(x_i, y_j, x, y, z) = \frac{1}{(x_i - x)^2 + (y_j - y)^2 + (z)^2} \qquad \text{(3D)} \qquad (10)$$

Next, a cross-correlation calculation of the super positioned source points to the measured voltage data at the electrodes.

$$\hat{C}(x, z) = \sum_i g(x_i, x, y, z) \times V_{measured}(x_i) \qquad \text{(2D)} \qquad (11)$$

$$\hat{C}(x, y, z) = \sum_i \sum_j g(x_i, y_j, x, y, z) \times V_{measured}(x_i, y_j) \qquad \text{(3D)} \qquad (12)$$

By multiplying g with the potential data $V_{measured}$, the resultant $\hat{C}$ is the sum of the observed potentials scaled by g.

Finally, a normalisation of the cross correlation coefficient allows for direct comparison of coefficients associated with sources at different depths:

$$C_{normalised}(x,z) = \frac{\hat{C}(x,z)}{\left[\sum_i g^2(x_i,x,y,z)\sum_i V^2_{measured}(x_i)\right]^{\frac{1}{2}}} \quad \text{(2D)} \quad (13)$$

$$C_{normalised}(x,y,z) = \frac{\hat{C}(x,y,z)}{\left[\sum_i\sum_j g^2(x_i,y_j,x,y,z)\sum_i\sum_j V^2_{measured}(x_i,y_j)\right]^{\frac{1}{2}}} \quad \text{(3D)} \quad (14)$$

This function results in a dimensionless correlation coefficient ranging from 0 to 1. Values close to 0 (poor correlations with the data), are positions that are unlikely to be elementary point sources contributing the measured signal.

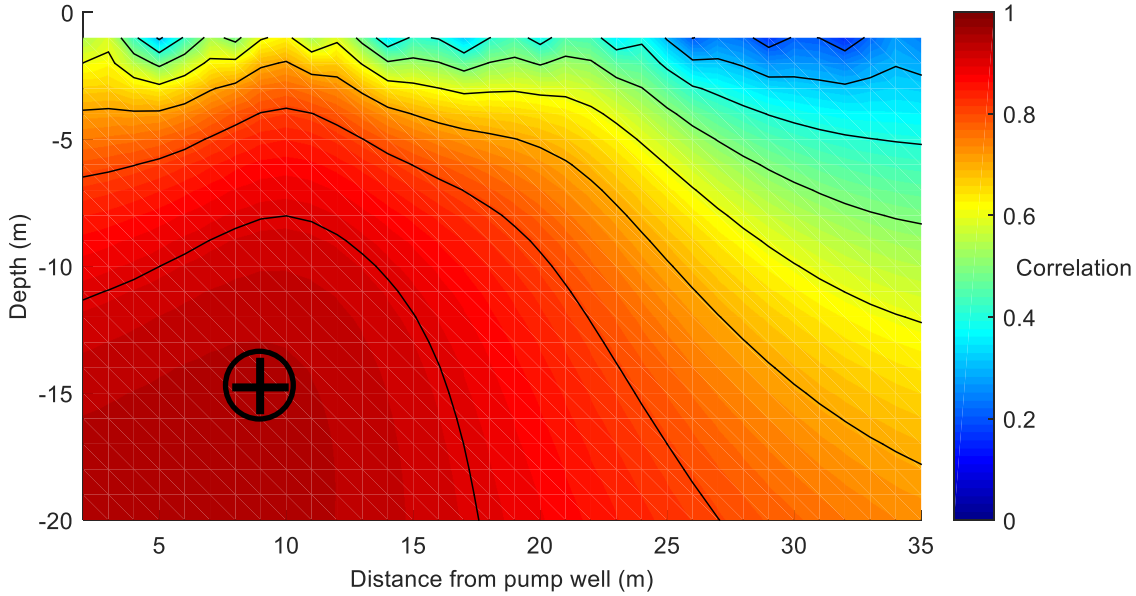

Figure 14: 2D tomographic image produced along Line 2 @14:20:00, to 20m depth. Shows highest correlations at depths of ~15m, quite proximal to the pumping well (~5-10m), marked by a cross. Correlation tapers off at greater distances.

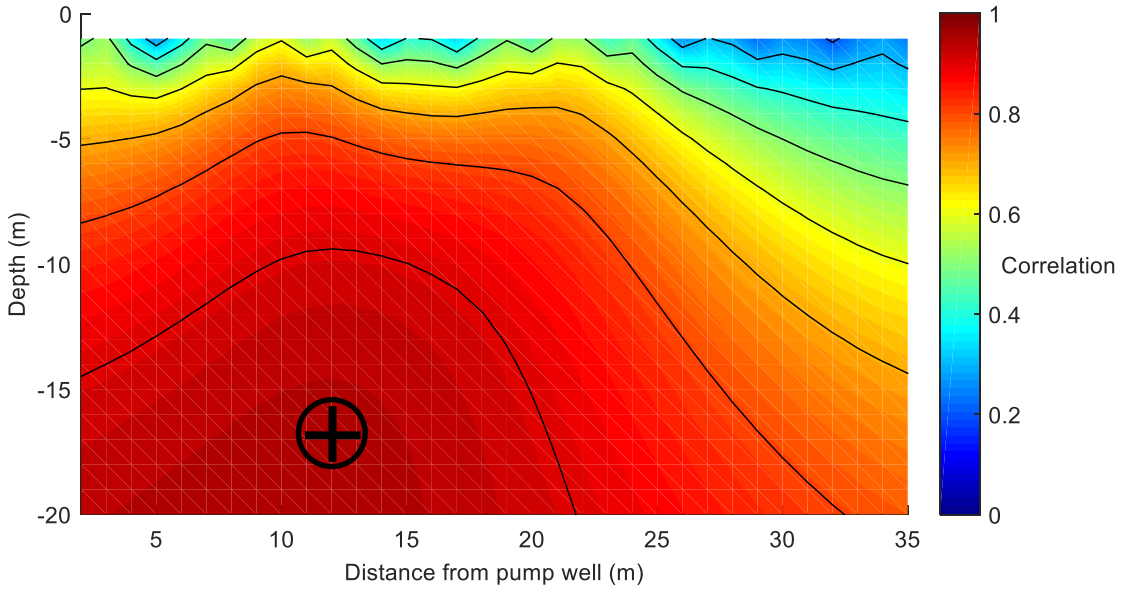

Figure 15: 2D tomographic image produced along Line 2 @14:40:00, to 20m depth. Shows highest correlations at depths of ~17m, but this time this high region has shifted slightly further away from the pump well (~12m laterally), marked by a cross. Correlation continues to taper off at greater distances.

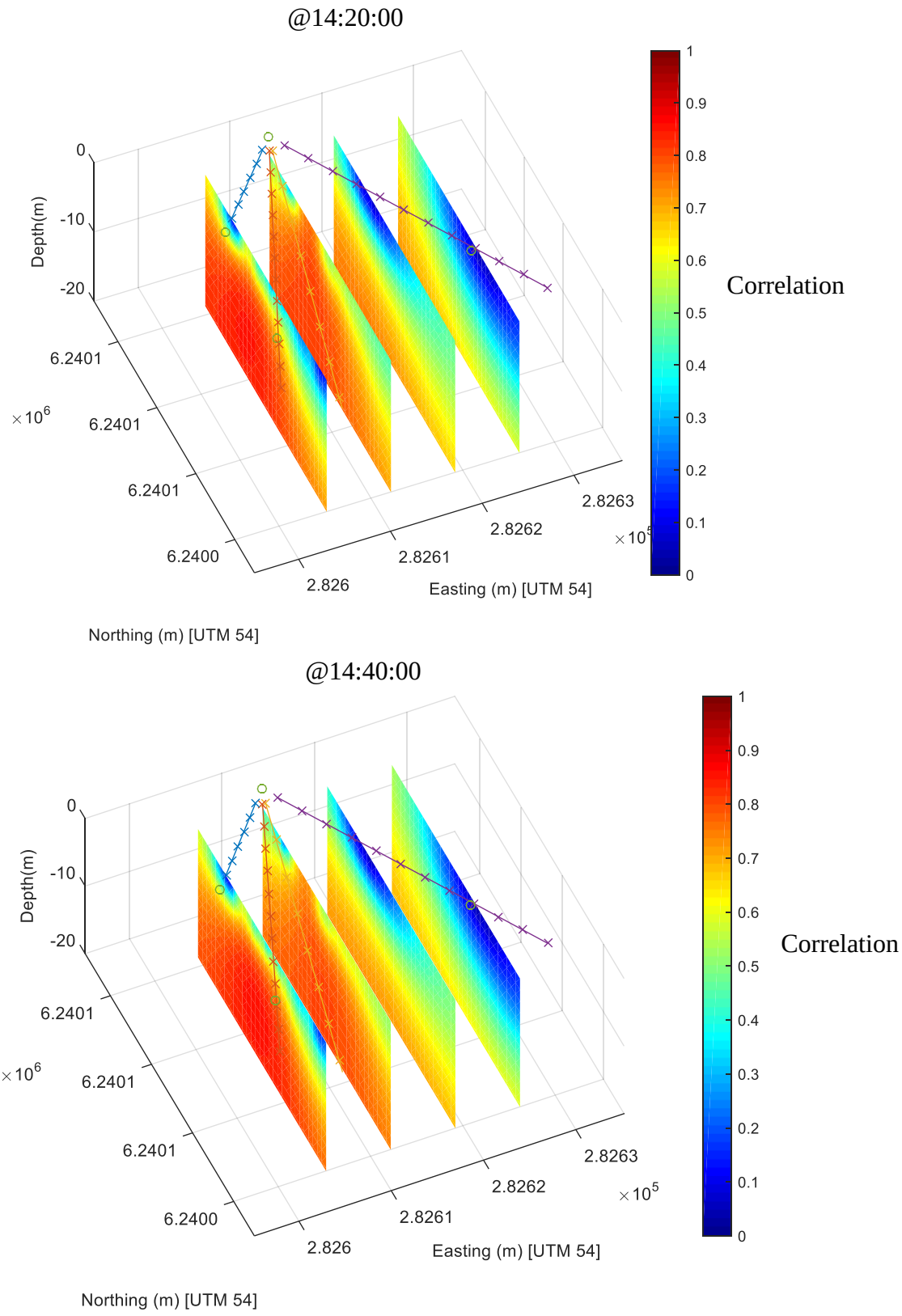

Figure 16: 3D Tomography profiles for ~14:20:00 (top) and ~14:40:00 (bottom). Side view with multiple slices. Region of high correlation evident between lines 2 and 3 similar to 2D tomography plots. This source appears to move between the two periods outwards along line 2.

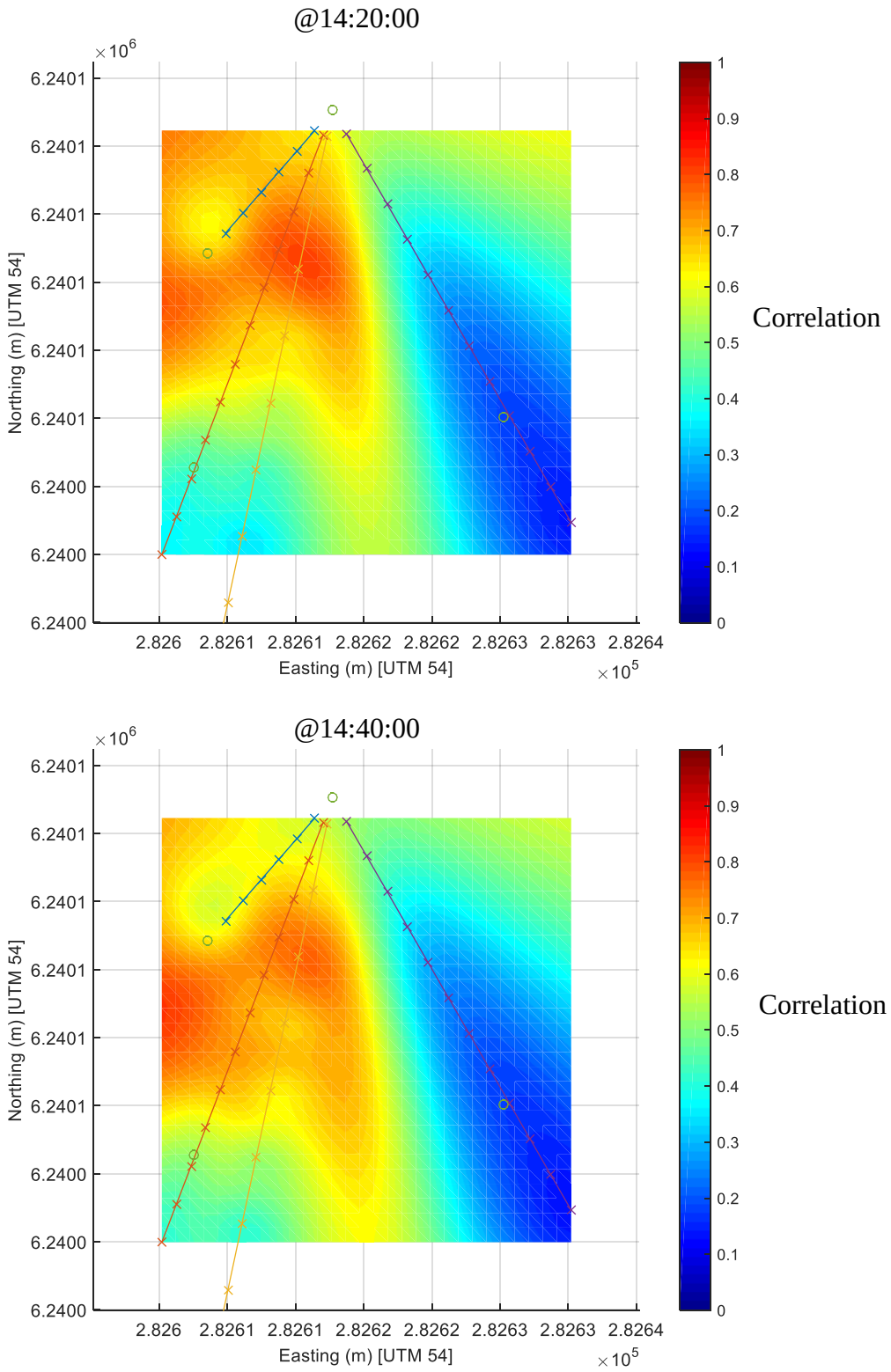

Figure 17: 3D Tomography profiles for ~14:20:00 (top) and ~14:40:00 (bottom). Top down view on a depth slice at 5m. This figure clearly demonstrates the slight lateral shift in the SP source along lines 2 and 3.

DISCUSSION

Electrodes that were particularly noisy were removed from the stack in Figures 6 to 9. The source of noise is unclear, but may be due to significant changes in contact resistances, as Lines 1 and 3 crossed a graded road.

Early-mid stage of pumping: 14:20:00 ACST

For the first pump test, beginning at 14:00:00 (ACST), Lines 1 through 3 begin to show an excursion from the previous baseline voltages, with the magnitude of these variations roughly correlating with both line orientation and electrode distances along each line (Figures 6 through 8). The level of these voltage differences from baseline broadly appears to be greatest at electrodes close to the pump well, with a reduction in amplitude at the more distal electrodes. At more distant locale, these electrodes likely approach the limits of the zone of influence of the pump test and fluid movement (Costar et al. 2008). Line 2 appears to show the greatest amplitude peaks in voltage excursions on average, in comparison to Line 1 and 3 which share lesser magnitudes. Line 4 (Figure 9) is the exception, showing no visible changes in the readings that seem to correlate with the beginning of pumping.

During this same early pump phase, relatively proximal electrode voltage recordings from each line were graphed next to each other in Figure 10. Here, unique electrodes from different lines, recorded using different SP logger boxes, have captured voltage information with highly similar characteristics, with the exception of Line 4 electrode 2. This similarity in data captured at comparable locations gives confidence that the data captured is not random noise and that there is some recordable signal at this location. Of interest is the variation in amplitude between these electrodes. From the map of site in

Figure 4, it can be seen that these electrodes vary in distance from each other ~3-6m, and yet there is some consistent variation in amplitude between Lines 1 to 3 (seen again later in Figure 12, and throughout the raw data plots in Figures 6-8). This level of change over such a small distance is interesting, and may either indicate very shallow anisotropy in water movement with a strong preference along the lineation of Line 2, or potentially small errors due to variance of individual electrode readings. The fact these larger amplitudes are observed along many of the electrodes of Line 2 however, as well as similar results for the end of pump line comparison in figure 13, reduces the likelihood of the latter argument.

The higher level variation in voltage along Line 2 can be seen in the change in voltage map in Figure 11 at 14:20:00, in map view. Line 2 shows a rough decrease in voltage amplitudes from baseline values at increased distances from the pump well, and average values higher than that of the other adjacent lines, particularly between electrodes 3-8. Line 1 and 3 also exhibit similar amplitudes to each other, but of a slightly lower magnitude than those observed in Line 2. Line 4, as expected from previous discussion, showed little variation.

Results from this section seem to suggest, from mere visual inspection, that there is some preferential lineation of voltage anomalies, likely associated with discrete flow in a SSW orientation from the pump well, centred along Line 2.

2D tomography was conducted along a profile coincident with Line 2 based on this hypothesis. Line 2 was host to the highest values of voltage variance from baseline

(assumed to be related to electrokinetic signal); with supporting physical drawdown measurements from Well 2, the only well to show any significant drawdown during pumping (see Appendix D). The early-mid period analysed at 14:20:00 shows a relative correlation high reasonably close to the pump well at a distance of ~10m laterally, and a depth maximum beginning around 14m depth (Figure 14). Here the tomography has identified a region of high correlation, laterally constrained within the first 8 or so electrodes along Line 2, and at a depth ranging from ~8m to the limit of the reliability of the tomography, in this instance around 16-20m.

Late stage of pumping: 14:40:00 ACST

Towards the end of the first pump test, around 14:40:00 ACST, there is a marked blip on the voltages for all lines with the exception of Line 4. This was of particular interest as it seemed well defined and a markedly discrete voltage pulse. Again this voltage difference from baseline broadly appears to be greatest at electrodes close to the pump well, and tapering off in amplitude along each line away from the pump well (Figure 13). Similar to the first time interval analysis, Line 2 shows the greatest amplitude to the signal in comparison to the other lines (Figure 13).

Figure 15 is the map of tomographic correlation values produced with the voltage excursions at this time period along Line 2. This shows a notable change in comparison to Figure 14 for the earlier pump values. The central region of highest correlation has shifted further outwards (initially ~ 15m depth and 8m lateral distance from pump), and is now centralised more around 12m distance out from the well, at a depth of ~17m. As the local central area around the pump well is drained with progressive pumping,

sources are likely being utilised at greater distances to compensate for the depletion of the proximal fluids (Jardani et al. 2006, Costar et al. 2008, Jardani et al. 2009), leading to a slightly more laterally extensive correlation high.

As the 2D tomography is limited to the single line of data, 3D tomography was also utilised to fully utilise the SP data set captured. This data produces similar trends seen in the 2D tomography. With this 3D map, the preferential direction of self-potential response is more evident, with the region between lines 1 and 3 the main area of high correlation response, with particular focus along Line 2 and 3. At depth slices of 5-10m in particular, this shows a region of high correlation initially very proximal to the pump well site @14:20:00 (Figure 17), transitioning further along the line and across more to Line 3 at the end of the pumping period @14:40:00 (Figure 17).

This sense of preferential flow path is agreeable with the known geological information of the area; dominant ~N^{th}-S^{th} oriented fractures associated with the syncline, as well as similarly striking bedding surfaces (Figure 2). These discrete pathways for flow have likely been the host of the main fluid flux associated with the pumping, and the SP results appear to have resolved this information. This data is consistent with previous studies on preferential flow related to geological environment constraints, in particular Revil et al. (2005), where preferential ground water flow pathways were seen in relation to a buried paleo-channel. Although the method by which the SP response was sourced (pumping test vs. natural paleochannel flow), the fundamental source of the voltage response was still electrokinetic in nature.

In relation to the hypotheses outlined earlier in this paper, it cannot be stated that the hydrogeological system is entirely understood in detail from SP alone, particularly with respect to the fractured rock environment. Although we did not see obvious, discrete packages of localised flow along sharp boundaries, we do see a preferential, non-radial pattern to the flow in the 2D, and 3D tomography in particular. This information is agreeable with physical drawdown measurements on the day, showing the only major scale drawdown was restricted to well 2 during the pumping (Appendix D), as well consistent with geological knowledge of the dominant fracture and bedding surface orientations.

Without these physical wells at the site to measure the drawdown, this information would not be available, and herein lays the potential benefits of the SP method. SP has, to some degree, been able to delineate broad preferential subsurface fluid movement in this study. The ease and cost of this method is its strength, as it is much simpler than drilling observation wells, and does not disturb the natural hydraulic environment.

Methodology improvements

With respect to the raw data; Line 4 (Figure 9) shows very strong correlation between electrodes, but exhibit only very small amplitude changes with respect to the other lines. It's possible this line might only be seeing regional inductive fields rather than electrokinetic signals, and that any signal is simply so small here, that it is at the noise level of the device. There is also the issue that Line 4 actually experienced slightly different electrical contact than the other lines with the ground. This line ran down the slight topography of the area, and the soil along this line was slightly waterlogged after

some previous day's rain. Potentially this moist soil led to a decrease in the contact resistance with the ground, and the voltages recorded have been 'muted' as a result.

In relation to the pumping itself, we never fully allowed the potentiometric surface to return to equilibrium on day 1 due to time constraints (Figure 5). As a result, the hydrogeological environment was always in a state of flow. To return to true equilibrium we needed to allow the water level in the pump well to return to initial values. This in-field error is arguably quite important in a fractured rock environment (more so than a homogeneous porous sedimentary aquifer), as major fluid movement will be restricted to discrete bedding surfaces and fracture plane intersections of the well (Figure 5). By not allowing the water levels to rise above these discrete points, meant these flow pathways were always in a state of flux.

For later surveys, it is recommended to use the 'Petiau' style non-polarizable electrodes (Petiau 2000) rather than the stakes used in this survey, as well as more work to ensure the electrical contact with the ground is as uniform as possible between individual electrodes and lines. The reasoning for this is to reconfirm the results found during this test, in particular the response seen in Line 4, and ensures this was not a result of the varied ground electrical contact due to the more water logged soil. Revil and Jardani (2013) suggest placing electrodes in a small hole filled with a bentonite mud. The advantage of this bentonite is that it maintains the potential drop between individual electrodes and the Earth, and remains relatively constant through time.

As well as the above, metal stakes are susceptible to electrochemical reactions at the metal-moisture interface. These reactions, as discussed previously, can also generate voltages and results in the build-up of charge on these stakes, potentially leading to false or unintelligible readings at the logger (Lowrie 2007). Using non-polarisable electrodes such as the Petiau type significantly reduces, if not completely removes, this effect (Petiau 2000). The period of the tests was relatively short, and it is unlikely over this time period that this had a significant effect, particularly as the stakes are galvanised and resistant to corrosion. Based on this assumption, as well as the limited time period allocated for installation of the equipment, they were utilised in this case. However for subsequent tests and any long period surveys, these metal stakes should not be deployed.

The layout of the lines with respect to the pump well was also less than ideal. It would have been preferred to map the voltages in a radial pattern surrounding the central pump well, however due to the location this was not possible due to the presence of a road and tennis courts to the North and North-West.

Tomography calculation assumptions

In the tomographic calculations, a major assumption is that the background resistivity is uniform. This is likely not the case, however without an accompanying electrical resistivity survey, this could not be avoided.

Due to the nature of the 3D tomographic plots, the tomography algorithm was left to extrapolate to regions at the bounding regions where there was little data to constrain it. This fact should be considered before the extremities of these plots are analysed. In particular, the 3D tomographic images show some strange values towards the

extremities of the bounds of the map, particularly north-east of Line 4 and out to the west of Line 1.

It is recommended that for future surveys, a location where the full radial profile about a central pump well is possible, to better constrain the tomography, and to understand the full hydrological system in 360° around the pump well. As well as this, time should be allocated to allow the full recovery phase of the potentiometric water table surface to occur, with measurements taken for the entire period. In particular, this method should be accompanied with a resistivity survey for the future, to be incorporated into the tomographic algorithm and provide improved accuracy for resolving likely SP source locations. An interesting aside would be to produce a moving image at any point in time, potentially even in real time, of the tomographic image modelling the potential source locations. This would allow better visualisation of the system as it changes in 4D.

CONCLUSIONS

This study has considered the viability of the SP method in a fractured rock media system, for monitoring groundwater flow and delineating preferential flow paths, and modelling potential source depths. These aims have been achieved using an SP survey at the Watervale site, South Australia, in conjunction with physical drawdown measurements of the water table at observation wells, and knowledge of the geological environment of the region.

Results from the field study indicate evident anisotropy in the voltages, in space and time. Through visual analysis of the data and tomographic methods, the SP signals seem

to have delineated, with some confidence, preferential flow pathways through the fractured rock media environment in a roughly N-S to NNE-SSW direction with respect to the pump well, centred on Line 2.

This information is agreeable with physical drawdown measurements on the day, showing the only major scale drawdown was restricted to well 2 during the pumping (Appendix D), as well consistent with geological knowledge of the dominant fracture and bedding surface orientations.

Along with this information, this report has imaged variations in the SP sources in 4D, with the central tomographic high appearing to shift through time, outwards from the pump along Lines 2 and 3. This is believed to be as a result of near pump sources becoming depleted and more laterally extensive sources initiating flow. Although more work needs to be undertaken to understand fractured rock aquifer responses in greater detail, these results are positive and lend credence to the viability of the SP method for use in fractured rock aquifers.

ACKNOWLEDGMENTS

To my supervisor, Graham Heinson, I am most thankful for the direction and support provided throughout the year. I would also like to thank Joseph Rugari for his insights and suggestions to my project, and assistance throughout the honours year, as well as his invaluable maintenance and management of the SP loggers. Warm thanks to Goran Boren for his work on modifying the SP equipment, as well as input and assistance in relation to the SP field survey.

REFERENCES

ARCHIE G. E. 1942. The Electrical Resistivity Log as an Aid in Determining Some Reservoir Characteristics. *Trans. AIME* **146**.

BOLÈVE A., REVIL A., JANOD F., MATTIUZZO J. L. & JARDANI A. 2007. Forward Modeling and validation of a new formulation to compute self-potential signals associated with ground water flow. *Hydrol. Earth Syst. Sci.* **11**, 1661-1671.

CORWIN R. F. & HOOVER D. B. 1979. The self-potential method in geothermal exploration. *Geophysics* **44**, 226-245.

COSTAR A., HEINSON G., WILSON T. & SMIT Z. 2008. Hydrogeophysical mapping of fracture orientation and groundwater flow in the Eastern Mount Lofty Ranges, South Australia. DWLBC Report 2009/09, Government of South Australia, through Department of Water, Land and Biodiversity Conservation, Adelaide

DARNET M., MAINEULT A. & MARQUIS G. 2004. On the origins of self-potential (SP) anomalies induced by water injections into geothermal reservoirs. *Geophysical Research Letters* **31**, p.L19609.

DI MAIO R. & PATELLA D. 1994. Self-potential anomaly generation in volcanic areas. The Mont Etna case history. *Acta Vulcanol.* **4**, 124-199.

FAGERLUND F. & HEINSON G. 2003. Detecting subsurface groundwater flow in fractured rock using self-potential (SP) methods. *Environmental Geology* **43**, 782-794.

HÄMMANN M., MAURER H. R., GREEN A. G. & HORSTMEYER H. 1997. Self-Potential Image Reconstruction: Capabilities and Limitations. *Journal of Environmental and Engineering Geophysics* **2**, 21-35.

HEINSON G. & SEGAWA J. 1997. Electrokinetic signature of the Nankai Trough accretionary complex: preliminary modelling for the Kaiko-Tokai program. *Physics of the Earth and Planetary Interiors* **99**, 33-53.

HISCOCK K. & BENSE V. 2014. Hydrogeology : Principles and Practice, 2nd ed. Wiley, Somerset, NJ, USA

ISHIDO T. & MIZUTANI H. 1981. Experimental and theoretical basis of electrokinetic phenomena in rock-water systems and its applications to geophysics. *Journal of Geophysical Research: Solid Earth* **86**, 1763-1775.

JARDANI A., REVIL A., AKOA F., SCHMUTZ M., FLORSCH N. & DUPONT J. P. 2006. Least squares inversion of self-potential (SP) data and application to the shallow flow of ground water in sinkholes. *Geophysical Research Letters* **33**, p.L19306.

JARDANI A., REVIL A., BOLÈVE A. & DUPONT J. P. 2008. Three-dimensional inversion of self-potential data used to constrain the pattern of groundwater flow in geothermal fields. *Journal of Geophysical Research: Solid Earth* **113**, p.B09204.

JARDANI A., REVIL A., BARRASH W., CRESPY A., RIZZO E., STRAFACE S., CARDIFF M., MALAMA B., MILLER C. & JOHNSON T. 2009. Reconstruction of the Water Table from Self-Potential Data: A Bayesian Approach. *Ground Water* **47**, 213-227.

LOVE A., COOK P., HARRINGTON G. & SIMMONS C. 2013. Groundwater flow in the Clare Valley. Department for Water Resources, Government of South Australia

LOWRIE W. 2007. Fundamentals of Geophysics. Cambridge University Press,

MAINEULT A., BERNABÉ Y. & ACKERER P. 2005. Detection of advected concentration and pH fronts from self-potential measurements. *Journal of Geophysical Research: Solid Earth* **110**, p.B11205.

MAINEULT A., STROBACH E. & RENNER J. 2008. Self-potential signals induced by periodic pumping tests. *Journal of Geophysical Research: Solid Earth* **113**, p.B01203.

MINSLEY B. J., SOGADE J. & MORGAN F. D. 2007. Three-dimensional source inversion of self-potential data. *Journal of Geophysical Research: Solid Earth* **112**, p.B02202.

MOORE J. R. & GLASER S. D. 2007. Self-potential observations during hydraulic fracturing. *Journal of Geophysical Research: Solid Earth* **112**, p.B02204.

MORGAN F. D., WILLIAMS E. & MADDEN T. 1989. Streaming potential properties of westerly granite with applications. *Journal of Geophysical Research* **94**, 12449-12461.

NAUDET V. & REVIL A. 2005. A sandbox experiment to investigate bacteria-mediated redox processes on self-potential signals. *Geophysical Research Letters* **32**, p.L11405.

NOURBEHECHT B. 1963. Irreversible thermodynamic effects in inhomogeneous media and their applications in certain geoelectric problems. PhD thesis. Massachusetts Institute of Technology, Cambridge, MA.

PETIAU G. 2000. Second Generation of Lead-lead Chloride Electrodes for Geophysical Applications. *pure and applied geophysics* **157**, 357-382.

REVIL A., PEZARD P. A. & GLOVER P. W. J. 1999a. Streaming potential in porous media: 1. Theory of the zeta potential. *Journal of Geophysical Research: Solid Earth* **104**, 20021-20031.

REVIL A., SCHWAEGER H., CATHLES L. M. & MANHARDT P. D. 1999b. Streaming potential in porous media: 2. Theory and application to geothermal systems. *Journal of Geophysical Research: Solid Earth* **104**, 20033-20048.

REVIL A., EHOUARNE L. & THYREAULT E. 2001. Tomography of self-potential anomalies of electrochemical nature. *Geophysical Research Letters* **28**, 4363-4366.

REVIL A., NAUDET V., NOUZARET J. & PESSEL M. 2003. Principles of electrography applied to self-potential electrokinetic sources and hydrogeological applications. *Water Resources Research* **39**, p.1114.

REVIL A., CARY L., FAN Q., FINIZOLA A. & TROLARD F. 2005. Self-potential signals associated with preferential ground water flow pathways in a buried paleo-channel. *Geophysical Research Letters* **32**, p.L07401.

REVIL A., GEVAUDAN C., LU N. & MAINEULT A. 2008. Hysteresis of the self-potential response associated with harmonic pumping tests. *Geophysical Research Letters* **35**, p.L16402.

REVIL A. & JARDANI A. 2013. The Self-Potential Method. Cambridge University Press,

REVIL A., KARAOULIS M., SRIVASTAVA S. & BYRDINA S. 2013. Thermoelectric self-potential and resistivity data localize the burning front of underground coal fires. *GEOPHYSICS* **78**, B259-B273.

RIZZO E., SUSKI B., REVIL A., STRAFACE S. & TROISI S. 2004. Self-potential signals associated with pumping tests experiments. *Journal of Geophysical Research: Solid Earth* **109**, p.B10203.

SAHIMI M. 2011. Characterization of Fractures, Fracture Networks, and Fractured Porous Media. *Flow and Transport in Porous Media and Fractured Rock,* pp. 143-177. Wiley-VCH Verlag GmbH & Co. KGaA.

SATO M. & MOONEY H. M. 1960. The electrochemical mechanism of sulfide self-potentials. *Geophysics* **25**, 226-249.

SOUEID AHMED A., JARDANI A., REVIL A. & DUPONT J. P. 2013. SP2DINV: A 2D forward and inverse code for streaming potential problems. *Computers & Geosciences* **59**, 9-16.

TITOV K., REVIL A., KONOSAVSKY P., STRAFACE S. & TROISI S. 2005. Numerical modelling of self-potential signals associated with a pumping test experiment. *Geophysical Journal International* **162**, 641-650.

WILLIAMS K. H., HUBBARD S. S. & BANFIELD J. F. 2007. Galvanic interpretation of self-potential signals associated with microbial sulfate-reduction. *Journal of Geophysical Research: Biogeosciences* **112**, p.G03019.

APPENDIX A: INTERVAL CALCULATIONS SCRIPT

```
%-------------------------------------------------------------------------

%                Self-Potential Time Interval script
%                            Matthew Gard

%-------------------------------------------------------------------------

%For a specified interval (time interval used to capture variation from a
%baseline) the code runs the following:

%- 2D tomography plot along Line 2
%- 3D tomography plot with specified depth/lateral slices
%- Map of voltage variations from baseline
%- Plots of voltage variations from baseline for each line
%- Plots the voltages recorded at close electrodes for visual comparison

%-------------------------------------------------------------------------

%Load data and map coordinates

close all
load('SP_Watervale_Interp_MedFilt60s_Variables')
load('SP_Watervale_Map_Variables')
```

Selecting the time period

```
%To calculate voltage variance from 'baseline', a range was manually
%selected that seemed to incorporate the peak as well as the baseline value
%(minimum), and then the max-min was calculated

%Select time period
    SPstart = find(commonTimestamp_day1==datetime('09-Sep-0115 14:12:00'));
    SPstop = find(commonTimestamp_day1==datetime('09-Sep-0115 14:35:00'));
    timeImportant = '14:20:00';


%Calculate variance from baseline for each electrode along each line:

    %SP1
    spdiff = zeros(12,2);
    diff = zeros(12,1);
    for i = 1:12
        if i==9||i==10||i==11||i==12||i==7||i==8
            %Remove noisy data
            diff(i)=NaN;
        else
            %Calculate variance from baseline
            SPData = SP1interp_day1(:,i);
            spdiff(i,:) = minmax(SPData(SPstart:SPstop)');
            diff(i) = abs(spdiff(i,1)-spdiff(i,2));
```

```
        end
    end
    differenceSP(:,1)=diff;

    %SP2
    spdiff = zeros(12,2);
    diff = zeros(12,1);
    for i = 1:12
        %Calculate variance from baseline
        SPData = SP2interp_day1(:,i);
        spdiff(i,:) = minmax(SPData(SPstart:SPstop)');
        diff(i) = abs(spdiff(i,1)-spdiff(i,2));
    end
    differenceSP(:,2)=diff;


    %SP3
    spdiff = zeros(12,2);
    diff = zeros(12,1);
    for i = 1:12
        if i==3||i==9||i==10||i==8||i==11||i==12
            %Remove noisy data
            diff(i)=NaN;
        else
            %Calculate variance from baseline
            SPData = SP3interp_day1(:,i);
            spdiff(i,:) = minmax(SPData(SPstart:SPstop)');
            diff(i) = abs(spdiff(i,1)-spdiff(i,2));
        end
    end
    differenceSP(:,3)=diff;

    %SP4
    spdiff = zeros(12,2);
    diff = zeros(12,1);
    for i = 1:12
        %Calculate variance from baseline
        SPData = SP4interp_day1(:,i);
        spdiff(i,:) = minmax(SPData(SPstart:SPstop)');
        diff(i) = abs(spdiff(i,1)-spdiff(i,2));
    end
    differenceSP(:,4)=diff;

    clearvars diff i spdiff
```

Map of region with voltage differences plotted as colour dots

```
str = sprintf('Map of voltage difference from baseline @%s - 9th Sept', timeImportant);

figure('Name',str,'NumberTitle','off','position', [100, 100, 800, 600])
    line1GPS_x=line1GPS(:,1);
    line1GPS_y=line1GPS(:,2);
    differenceSP_1 = differenceSP(:,1);
```

```
    line2GPS_x=line2GPS(:,1);
    line2GPS_y=line2GPS(:,2);
    differenceSP_2 = differenceSP(:,2);

    line3GPS_x=line3GPS(:,1);
    line3GPS_y=line3GPS(:,2);
    differenceSP_3 = differenceSP(:,3);

    line4GPS_x=line4GPS(:,1);
    line4GPS_y=line4GPS(:,2);
    differenceSP_4 = differenceSP(:,4);

    %Plot electrode coordinates with respective voltage variance from
    %baseline calculated in previous section

scatter(line1GPS_x(~isnan(differenceSP_1)),line1GPS_y(~isnan(differenceSP_1)),75,differe
nceSP_1(~isnan(differenceSP_1)),'filled')
    hold on

scatter(line2GPS_x(~isnan(differenceSP_2)),line2GPS_y(~isnan(differenceSP_2)),75,differe
nceSP_2(~isnan(differenceSP_2)),'filled')

scatter(line3GPS_x(~isnan(differenceSP_3)),line3GPS_y(~isnan(differenceSP_3)),75,differe
nceSP_3(~isnan(differenceSP_3)),'filled')

scatter(line4GPS_x(~isnan(differenceSP_4)),line4GPS_y(~isnan(differenceSP_4)),75,differe
nceSP_4(~isnan(differenceSP_4)),'filled')
    hold off

    %Plot settings
    caxis([min(differenceSP(:))*1.1 max(differenceSP(:))*0.9])
    colormap parula
    h=colorbar;
    ylabel(h,'Voltage (mV)','rot', 0,'Position',[3 5.7])
    xTickValues = (282580:20:282640);
    yTickValues = (6240020:20:6240080);
    axis([xTickValues(1)+10 xTickValues(end) yTickValues(1)+10 yTickValues(end)])
    set(gca,'xTick',xTickValues)
    set(gca,'yTick',yTickValues)
    set(gca,'XTickLabel',sprintf('%3.4d\n',xTickValues))
    set(gca,'YTickLabel',sprintf('%3.4d\n',yTickValues))
    legend('Line 1','Line 2','Line 3','Line 4')
    grid on
    xlabel ('Easting (m)')
    ylabel ('Northing (m)')
    daspect([1 1 1])

    clearvars line1GPS_x line1GPS_y line2GPS_x line2GPS_y line3GPS_x ...
        line3GPS_y line4GPS_x line4GPS_y differenceSP_1 differenceSP_2 ...
        differenceSP_3 differenceSP_4 xTickValues yTickValues

    fig=gcf;
    set(findall(fig,'-property','FontSize'),'FontSize',12)
```

2D tomography and plot

```
%Select the line for the 2D tomography section
lineNo = 2;

%Calculate the distances from the pump well for each electrode
    xk=zeros(12,1);
    for i=1:12
            xk(i,1) = sum(lineDistances(lineNo,1:i));
    end

%Run the 2D tomography script with the coordinates of the electrodes and
%the voltage variances
[Tomo_2D,meshX,meshZ]=SP_Watervale_Tomo_2D(xk,differenceSP(:,lineNo));


%Plot the normalised result as a surface and contour plot
    str = sprintf('2D Tomography, line %d @%s - 9th Sept', lineNo,timeImportant);
    figure('Name',str,'NumberTitle','off','position', [100, 100, 800, 600])
    hold on
    surf(meshX',meshZ',zeros(size(Tomo_2D)),Tomo_2D)
    xlim([2, max(meshX(:))])
    ylim([min(meshZ(:)), 0])
    shading interp
    caxis([0 1])
    colormap jet
    xlabel ('Distance from pump well (m)');
    ylabel ('Depth (m)')
    h=colorbar;
    ylabel(h,'Correlation','rot', 0,'Position',[3 0.53])
    contour(meshX,meshZ,Tomo_2D','k')
    hold off
    daspect([1 1 1])

    fig=gcf;
    set(findall(fig,'-property','FontSize'),'FontSize',12)
```

3D tomography and plot

```
str = sprintf('3D Tomography @%s - 9th Sept', timeImportant);

%3D tomography code requires vertically concatenated data
    data =
vertcat(differenceSP(:,1),differenceSP(:,2),differenceSP(:,3),differenceSP(:,4));
    xdata = vertcat(line1GPS(:,1),line2GPS(:,1),line3GPS(:,1),line4GPS(:,1));
    ydata = vertcat(line1GPS(:,2),line2GPS(:,2),line3GPS(:,2),line4GPS(:,2));

%Remove data which is set as NaN (removed as noisy)
    xdata = xdata(~any(isnan(data),2),:);
```

```
    ydata = ydata(~any(isnan(data),2),:);
    data = data(~any(isnan(data),2),:);

%Run the 3D tomography code with the coordinates and voltage variance from
%baseline for the respective electrodes
    [SSAtrix,XI,YI,ZI] = SSA(xdata,ydata,data);

    [X,Y,Z]=meshgrid(XI,YI,ZI);


figure('Name',str,'NumberTitle','off','position', [100, 100, 800, 600])

%Determine slices to show in 3D plot
    xslice = [min(xdata)+5:7:max(xdata)];
    yslice = [0];
    zslice = [0];

%Plot the 3D slice map of 3D tomographic values
    slice(X,Y,Z,SSAtrix,xslice,yslice,zslice)
    shading interp
    caxis([0 1])
    colormap jet
    hold on
    plot(line1GPS(1:6,1),line1GPS(1:6,2),'-x',...
        line2GPS(:,1),line2GPS(:,2),'-x',...
        line3GPS(:,1),line3GPS(:,2),'-x',...
        line4GPS(:,1),line4GPS(:,2),'-x',...
        wellsGPS(:,1), wellsGPS(:,2),'o');
    hold off
    xlim([min(xdata)-5, max(xdata)+5])
    ylim([min(ydata)-5, max(ydata)+5])
    zlim([-20,0])
    xlabel ('Easting (m) [UTM 54]');
    ylabel ('Northing (m) [UTM 54]')
    zlabel('Depth(m)')
    daspect([1 1 1])
    view([0 90])


    fig=gcf;
    set(findall(fig,'-property','FontSize'),'FontSize',12)
```

Comparing close electrodes visually

```
str = sprintf('Comparing voltages for proximal electrodes @%s - 9th Sept',
timeImportant);

    figure('Name',str,'NumberTitle','off','position', [100, 100, 800, 600])
    hold on
    count = 1;
    %SP1 - Electrode 3
```

```
    plot(commonTimestamp_day1,SP1interp_day1(:,3)-mean(SP1interp_day1(:,3))+(0))
    hold on

    %SP2 - Electrode 3
    plot(commonTimestamp_day1,SP2interp_day1(:,3)-mean(SP2interp_day1(:,3))+(8))

    %SP3 - Electrode 2
    plot(commonTimestamp_day1,SP3interp_day1(:,2)-mean(SP3interp_day1(:,2))+(16))

    %SP4 - Electrode 2
    plot(commonTimestamp_day1,SP4interp_day1(:,2)-mean(SP4interp_day1(:,2))+(24))

    hold off

%Plot settings
    legend('Line 1 - Electrode 3','Line 2 - Electrode 3','Line 3 - Electrode 2','Line 4
- Electrode 2')
    grid on
    xlabel ('Time (hour)');
    ylabel ('Voltage (mV)')
    xlim([datenum(commonTimestamp_day1(SPstart)) datenum(commonTimestamp_day1(SPstop))])
    ylim([-5, 30])
    fig=gcf;
    set(findall(fig,'-property','FontSize'),'FontSize',12)
```

Voltage excursions for each electrode along the 4 lines

```
%Subplots to show each line and the voltage trends along them

str = sprintf('Voltage difference from baseline per electrode @%s - 9th Sept',
timeImportant);
figure('Name',str,'NumberTitle','off','position', [100, 100, 800, 600])


%Line 1 Plot
h=subplot(2,2,1);
plot(sqrt((line1GPS(:,1)-line1GPS(1,1)).^2+(line1GPS(:,2)-
line1GPS(1,2)).^2),differenceSP(:,1),'-o')
title ('Line 1');
xlabel ('Distance from electrode 1 (m)');
ylabel ('Voltage (mV)')
ylim([0 ceil(max(differenceSP(:)))])
set(h, 'position', [0.13 0.55 0.33 0.33])

%Line 2 Plot
h=subplot(2,2,2);
plot(sqrt((line2GPS(:,1)-line2GPS(1,1)).^2+(line2GPS(:,2)-
line2GPS(1,2)).^2),differenceSP(:,2),'-o')
title ('Line 2');
xlabel ('Distance from electrode 1 (m)');
ylabel ('Voltage (mV)')
```

```
ylim([0 ceil(max(differenceSP(:)))])
set(h, 'position', [0.57 0.55 0.33 0.33])

%Line 3 Plot
h=subplot(2,2,3);
plot(sqrt((line3GPS(:,1)-line3GPS(1,1)).^2+(line3GPS(:,2)-
line3GPS(1,2)).^2),differenceSP(:,3),'-o')
title ('Line 3');
xlabel ('Distance from electrode 1 (m)');
ylabel ('Voltage (mV)')
ylim([0 ceil(max(differenceSP(:)))])
set(h, 'position', [0.13 0.075 0.33 0.33])

%Line 4 Plot
h=subplot(2,2,4);
plot(sqrt((line4GPS(:,1)-line4GPS(1,1)).^2+(line4GPS(:,2)-
line4GPS(1,2)).^2),differenceSP(:,4),'-o')
title ('Line 4');
xlabel ('Distance from electrode 1 (m)');
ylabel ('Voltage (mV)')
ylim([0 ceil(max(differenceSP(:)))])
set(h, 'position', [0.57 0.075 0.33 0.33])


ha = axes('Position',[0 0 1 1],'Xlim',[0 1],'Ylim',[0
1],'Box','off','Visible','off','Units','normalized', 'clipping' , 'off');

text(0.5, 1,str,'HorizontalAlignment','center','VerticalAlignment', 'top','FontSize',
12)
```

Published with MATLAB® R2015a

APPENDIX B: 2D TOMOGRAPHY FUNCTION

```
function [Tomo_2D,meshX,meshZ] = SP_Watervale_Tomo_2D(xk,delta_Vobs)

%Check for NaN data and remove from result
    delta_Vobs = delta_Vobs(~any(isnan(delta_Vobs),2),:);
    xk = xk(~any(isnan(delta_Vobs),2),:);

    delta_Vobs=delta_Vobs';

%x and z axis mesh points to check for correlation with surface SP signals
%Note: dont make meshz depth more than half of meshx
    meshx = (0:1:max(xk));
    meshz = (-1:-1:-20);

%Initialise C_hat, C_norm and delta_Vcalc sizes for speed
    C_hat = zeros(length(meshx),length(meshz));
    C_norm = C_hat;
    delta_Vcalc=zeros(length(xk),length(meshx),length(meshz));

%Calculate delta_Vcalc for all xk at a given xi and zj
%Then calculates C_hat and C_norm at the given xi and zj
%Formula adapted from Hamman et al. 1997 - see description in thesis
    for i = 1:length(meshx)
        for j = 1:length(meshz)
            for k = 1:length(xk)
                  delta_Vcalc(k,i,j) = (1)/((xk(k)-meshx(i))^2+(-meshz(j))^2);
            end
            C_hat(i,j) = delta_Vobs*delta_Vcalc(:,i,j);
            C_norm(i,j) =
C_hat(i,j)/sqrt(sum(delta_Vcalc(:,i,j).^2).*sum(delta_Vobs.^2));
        end
    end

    Tomo_2D = C_norm;
    [meshX, meshZ] = meshgrid(meshx,meshz);
end
```

Published with MATLAB® R2015a

APPENDIX C: 3D TOMOGRAPHY FUNCTION

```
function [SSAtrix,XI,YI,ZI] = SSA(xdata,ydata,data)

%Define the spacing for the grid of elementary point sources
    xlin = 30;
    ylin = xlin;
    zlin = xlin;

%Set the grids
    amax = linspace(min(xdata),max(xdata),xlin);
    bmax = linspace(min(ydata),max(ydata),ylin);
%Depth grid manually defined - choose a depth. Must begin at a depth <0
%and depth!= 0 to avoid errors.
    cmax = linspace(-50,-0.0005,zlin);
    srow = length(data);



    for a=1:length(amax)
        for b=1:length(bmax)
            for c=1:length(cmax)
                for v=1:srow
                    %Scanner function
                    g(v)=1/((cmax(c))^2+(xdata(v)-amax(a))^2+(ydata(v)-bmax(b))^2);
                end
                %Correlation algorithm
                chat = sum(g'.*data);
                cnorm = sqrt((sum(g.^2))*(sum(data.^2)));
                SSAtrix(b,a,c)=chat/cnorm;
            end
        end
    end


    [i, j, k] = size(SSAtrix);
    XI=linspace(min(xdata),max(xdata),j);
    YI=linspace(min(ydata),max(ydata),i);
    ZI=linspace(-50,-1,k);
end
```

Published with MATLAB® R2015a

Appendix D: Physical Well Drawdown Observations

Watervale Pump Test- Well Drawdown Observation's

Day 1

date: 9/09/2015

SP1		SP2		SP3		SP4	
time (24hrs)	70m depth	time	70m depth	time	70m depth	time	70m depth
1400	7.16	1400	7.40	1400	7.43	1400	5.74
1406	7.16	1408	7.41	1405	7.43	1700	5.74
1412	7.17	1413	7.54	1410	7.44		
1417	7.17	1419	7.76	1450	7.44		
1422	7.17	1425	8.20	1455	7.43		
1427	7.17	1430	8.45	1700	7.43		
1431	7.17	1435	8.86				
1438	7.17	1440	9.18				
1445	7.17	1447	9.53				
1451	7.17	1452	9.70				
1456	7.17	1458	9.84				
1502	7.17	1503	9.93				
1508	7.17	1509	9.97				
1516	7.17	1515	9.99				
1601	7.17	1520	9.98				
1700	7.17	1529	9.91				
		1536	9.84				
		1541	9.77				
		1546	9.71				
		1551	9.63				
		1555	9.57				
		1600	9.49				
		1606	9.38				
		1612	9.28				
		1616	9.22				
		1621	9.21				
		1627	9.28				
		1632	9.38				
		1638	9.52				
		1643	9.63				
		1648	9.80				
		1653	9.91				
		1658	10.01				
		1703	10.08				
		1708	10.13				
		1714	10.14				
		1719	10.14				